Crystal structures and magnetic properties of rare earth tantalates RE_3TaO_7 (RE = rare earths)

2004 J. Phys.: Condens. Matter 16 4103

(http://iopscience.iop.org/0953-8984/16/23/025)

INSTITUTE OF PHYSICS PUBLISHING JOURNAL OF PHYSICS: CONDENSED MATTER

J. Phys.: Condens. Matter **16** (2004) 4103–4120 PII: S0953-8984(04)77585-2

Crystal structures and magnetic properties of rare earth tantalates RE_3TaO_7 (RE = rare earths)

Makoto Wakeshima, Hiroaki Nishimine and Yukio Hinatsu

Division of Chemistry, Graduate School of Science, Hokkaido University, Sapporo 060-0810, Japan

Received 9 March 2004
Published 28 May 2004
Online at stacks.iop.org/JPhysCM/16/4103
DOI: 10.1088/0953-8984/16/23/025

Abstract

The crystal structures and magnetic properties of rare earth tantalates RE_3TaO_7 (RE = rare earths) are reported. Their crystal structures were grouped into three types: La_3NbO_7-type, Y_3TaO_7-type, and defect-fluorite-type. For the Ho_3TaO_7 compound, two different phases (Y_3TaO_7-type and defect-fluorite-type) were prepared. At around room temperature, Nd_3TaO_7 was found to transform from the Y_3TaO_7-type phase to La_3NbO_7-type phase with increasing temperature.

Temperature dependences of the magnetic susceptibilities and specific heats indicated that the Nd and Tb compounds undergo a 'two-step' antiferromagnetic transition with separate ordering of ions on different crystallographic sites below 2.6 and 3.6 K, respectively. The Dy^{3+} ion was found to be in an antiferromagnetic state below 2.3 K. The Ho_3TaO_7 with the Y_3TaO_7-type structure showed an antiferromagnetic-like transition, while no magnetic ordering was observed down to 1.8 K for the defect-fluorite-type Ho_3TaO_7.

1. Introduction

Rare earth tantalates RE_3TaO_7 (RE = rare earths) show polymorphic modifications based on a fluorite-type lattice. The RE_3TaO_7 compounds containing small rare earth ions (RE = Ho–Lu) have a defect-fluorite-type cubic structure in which RE and Ta ions randomly occupy the cation sites in the molar ratio of 3:1 [1–8]. The RE_3TaO_7 compounds with RE^{3+} larger than Ho^{3+} crystallize in an orthorhombic weberite-type supercell with dimensions $a \sim 2a_{\text{fluorite}}$, $b \sim c \sim \sqrt{2}a_{\text{fluorite}}$ [5–8]. For this weberite-type RE_3TaO_7, the oxide vacancies order on the anion sites, and the RE and Ta ions occupy the cation sites regularly. The Ta^{5+} cations are octahedrally coordinated and the TaO_6 octahedra share corners forming an infinite one-dimensional zig-zag chain parallel to the c-axis. The crystal structures of the weberite-type RE_3TaO_7 are grouped into two types, and their space groups are $Cmcm$ (La_3NbO_7-type) for the large RE^{3+} (RE = La, Pr) ions and $C222_1$ (Y_3TaO_7-type) for the medium-size RE^{3+} (RE = Y,

Nd–Ho) ions. For some RE_3TaO_7, both the Y_3TaO_7-type phase and the defect-fluorite-type phase can be prepared under different heating conditions [6–8].

From the viewpoint of their one-dimensional feature, interesting electrical and magnetic properties are expected for the weberite-type RE_3MO_7 compounds, and many researchers have investigated these for various RE ions and M = Mo, Ru, Ir, Os and Re [9–22]. In these cases, both the paramagnetic RE^{3+} and M^{5+} ions contribute to the magnetic properties of RE_3MO_7 compounds, and their magnetic behaviour is complicated.

In order to elucidate the magnetic contribution of the RE^{3+} ions at low temperatures in the weberite-type compounds, we have investigated the magnetic properties of rare earth tantalates RE_3TaO_7 in which the Ta^{5+} ions are diamagnetic. For this series of RE_3TaO_7, there is only one report that Pr_3TaO_7 is paramagnetic down to ∼4 K [10]. In this paper, we report the results of magnetic susceptibility and specific heat measurements on RE_3TaO_7 in the temperature range of 1.8–400 K.

2. Experimental details

A series of RE_3TaO_7 (RE = rare earths) was synthesized by a solid-state reaction process. Powders of tantalum oxide (Ta_2O_5) and rare earth sesquioxide RE_2O_3 except for RE = Pr and Tb, each with a purity of more than 99.9% were used as starting materials. In the case of RE = Pr and Tb, Pr_6O_{11} and Tb_4O_7 were used. In order to remove any moisture, La_2O_3 and Nd_2O_3 were preheated in air at 1173 K. The stoichiometric mixtures except for RE = Ho were ground, pelletized and heated in air at 1673–1873 K for 12 h. The products were annealed at 1673–1873 K with several intermediate regrindings and repelletizings until a single RE_3TaO_7 phase was obtained. For the preparations of Ho_3TaO_7, the Y_3TaO_7-type and defect-fluorite-type phases were annealed at 1673 K for 240 h and at 1923 K for 72 h, respectively, and then were rapidly cooled down to room temperature (RT) in air.

The x-ray diffraction (XRD) measurements were carried out at RT in the range $10° \leqslant 2\theta \leqslant 120°$ using a 2θ step size of 0.02° with Cu Kα radiation monochromatized with curved graphite on a Rigaku RINT2200 diffractometer. For some compounds, the XRD profiles were obtained in the temperature range from 15 to 500 K. The Rietveld analyses were carried out with the program RIETAN-2000 [23] using collected diffraction data.

The temperature dependence of the magnetic susceptibilities was measured under both the zero-field-cooled condition (ZFC) and the field-cooled condition (FC) in the temperature range between 1.8 and 400 K by using a SQUID magnetometer (Quantum Design, MPMS-5S). The ZFC susceptibility measurements were performed under an applied magnetic field of 0.1 T, after the sample was cooled from room temperature to 1.8 K in zero field. For FC susceptibility measurements, the sample was cooled in the presence of a field of 0.1 T. For the Ho_3TaO_7 compound with the Y_3TaO_7-type structure, the magnetization measurements were performed up to 9 T at 1.8 and 5 K with a Quantum Design PPMS system.

For some compounds showing a magnetic anomaly, the specific heat measurements were carried out using a relaxation technique supplied by the commercial heat capacity measurement system (Quantum Design, PPMS) in the temperature range from 1.8 to 300 K. The sample in the form of a pellet (∼10 mg) was mounted on an alumina plate with Apiezon for better thermal contact.

3. Results and discussion

3.1. Crystal structures

Except for RE = Nd, all the RE_3TaO_7 compounds were obtained as a single phase. From the powder XRD profiles at RT, their structures are grouped into following three structural types:

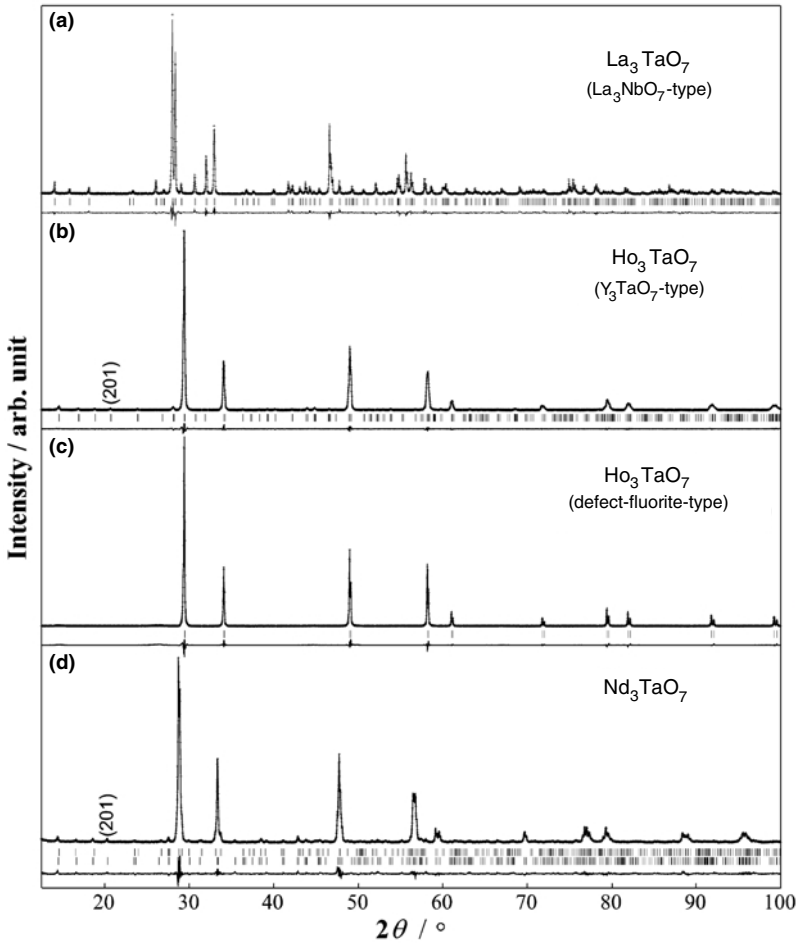

Figure 1. X-ray diffraction profiles for (a) La_3TaO_7, (b) Ho_3TaO_7 with Y_3TaO_7-type structure, (c) Ho_3TaO_7 with defect-fluorite-type structure, and (d) Nd_3TaO_7. The calculated and observed diffraction profiles are shown on the top solid line and cross markers, respectively. The vertical marks in the middle show positions calculated for Bragg reflections. The bottom trace is a plot of the difference between calculated and observed intensities. For Nd_3TaO_7, the upper vertical marks show the positions for the La_3NbO_7-type structure and the lower vertical marks show the positions for Y_3TaO_7-type structure.

RE = La, Pr: La_3NbO_7-type (space group: $Cmcm$),
RE = Sm–Ho: Y_3TaO_7-type (space group: $C222_1$),
RE = Ho–Lu: defect-fluorite-type (space group: $Fm\bar{3}m$).

For Ho_3TaO_7, two different phases (Y_3TaO_7-type and defect-fluorite-type) were prepared. Figures 1(a)–(c) show the typical diffraction profiles for the three structural types. In the profile of La_3TaO_7 with the La_3NbO_7-type structure, $h0l$ reflections with odd l are absent, whereas weak $h0l$ reflections are observed in that of Ho_3TaO_7 with the Y_3TaO_7-type structure. We have performed a Rietveld analysis with the program RIETAN-2000 for the diffraction profiles of all compounds. The refined lattice and positional parameters are listed in tables 1 and 2, respectively. These lattice parameters are in good agreement with those reported previously [1–8].

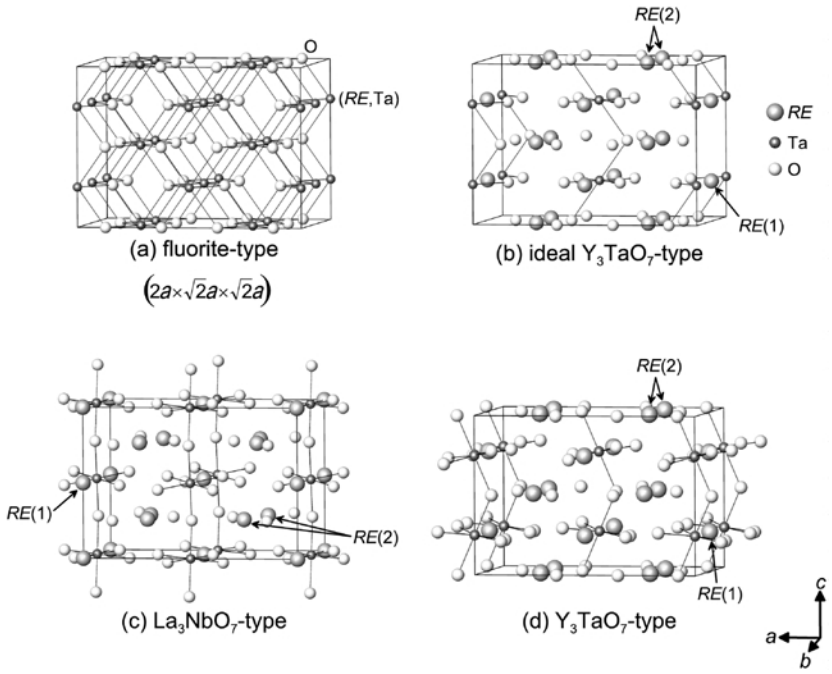

Figure 2. The schematic crystal structures of the RE_3TaO_7 compounds. (a): Fluorite-type (b): ideal Y_3TaO_7-type, (c): La_3NbO_7-type, and (d): Y_3TaO_7-type structure.

Table 1. Lattice parameters and R factors of RE_3TaO_7 at room temperature. (Note: $R_{wp} = \left[\sum_i w_i (y_i - f_i(x))^2 / \sum_i w_i y_i^2\right]^{1/2}$ and $R_I = \sum |I_k(o) - I_k(c)| / \sum I_k(o)$.)

RE	Type	a (Å)	b (Å)	c (Å)	R_{wp} (%)	R_I (%)
La	La_3NbO_7	11.1863(4)	7.6152(3)	7.7556(3)	13.81	4.12
Pr	La_3NbO_7	10.9910(4)	7.5094(3)	7.6788(3)	12.81	5.74
Nd	La_3NbO_7	10.9131(4)	7.5153(3)	7.6525(3)	15.62	4.70
Nd	Y_3TaO_7	10.8326(4)	7.6171(3)	7.6864(3)	15.62	2.25
Sm	Y_3TaO_7	10.7151(4)	7.5380(3)	7.6111(3)	9.02	2.27
Eu	Y_3TaO_7	10.6632(3)	7.5163(2)	7.5822(2)	9.27	1.97
Gd	Y_3TaO_7	10.6259(4)	7.5234(3)	7.5446(3)	7.67	2.45
Tb	Y_3TaO_7	10.5730(4)	7.4758(3)	7.5146(2)	7.18	1.74
Dy	Y_3TaO_7	10.5332(3)	7.4447(2)	7.4816(2)	7.75	1.63
Ho	Y_3TaO_7	10.4873(4)	7.4292(3)	7.4499(3)	6.83	1.69
Ho	Defect-fluorite	5.2599(2)			9.39	1.88
Er	Defect-fluorite	5.2328(2)			7.24	1.19
Tm	Defect-fluorite	5.2104(2)			7.04	1.35
Yb	Defect-fluorite	5.1956(2)			8.65	1.37
Lu	Defect-fluorite	5.1831(2)			8.73	1.77

Schematic crystal structures of RE_3TaO_7 compounds are illustrated in figures 2(a)–(d). Figure 2(a) shows the fluorite-type structure. In the defect-fluorite-type compounds, one-eighth of the oxide ions are randomly defective at the anion sites. For the ideal Y_3TaO_7-type structure, the specified anion sites in the fluorite-type structure are vacant, and the RE and Ta ions are arranged regularly in the ratio of 3:1 (see figure 2(b)). In the real Y_3TaO_7-type

Table 2. Positional parameters for La_3TaO_7 and Ho_3TaO_7.

	Site	x	y	z	B (Å^2)
La_3TaO_7					
La(1)	4a	0	0	0	0.67(4)
La(2)	8g	0.2261(1)	0.2992(2)	1/4	0.67
Ta	4b	0	1/2	0	0.20(5)
O(1)	4c	0	0.439(3)	1/4	0.7(2)
O(2)	16h	0.118(1)	0.321(1)	−0.045(1)	0.7
O(3)	8g	0.169(1)	0.027(2)	1/4	0.7
Y_3TaO_7-type Ho_3TaO_7					
Ho(1)	4b	0	0.4956(2)	1/4	1.15(5)
Ho(2)	8c	0.2360(2)	0.2374(2)	0	1.15
Ta	4b	0	0	1/4	0.69(7)
O(1)	8c	0.139(2)	0.181(2)	0.304(3)	0.7(1)
O(2)	8c	0.121(2)	0.770(2)	0.267(2)	0.7
O(3)	4a	0.131(2)	1/2	0	0.7
O(4)	4a	0.131(2)	1/2	1/2	0.7
O(5)	4a	0.072(2)	0	0	0.7
Defect-fluorite-type Ho_3TaO_7					
Ho/Ta	4a	0	0	0	1.2(5)
O	8b	1/4	1/4	1/4	6.3(3)

compound, the Ta ions attract the adjacent oxide ions and the crystal structure is distorted to be orthorhombic (see figure 2(d)). For Ho_3TaO_7 prepared in this study, high-temperature heating at 1923 K caused the disordering of the Ho and Ta ions at the cation sites and the formation of irregular oxide-ion vacancies (defect-fluorite-type structure), while the product annealed at 1673 K was crystallized in the Y_3TaO_7-type structure.

The La_3NbO_7-type and Y_3TaO_7-type structures have similar features, as shown in figures 2(c) and (d). The TaO_6 octahedra share the O(3) (La_3NbO_7-type) and O(5) (Y_3TaO_7-type) ions and form an infinite one-dimensional zig-zag chain parallel to the ⟨001⟩ direction. The RE(1) ions are coordinated by eight oxide ions and the distorted $RE(1)O_8$ cubes also form an one-dimensional chain through edge-sharing. The TaO_6 and $RE(1)O_8$ chains lie alternately parallel to the (010) plane, and the RE(2) ions are 7-coordinated by oxide ions between the slabs consisting of these chains. For these weberite-type structures, the TaO_6 octahedron and $RE(1)O_8$ cube in the La_3NbO_7-type structure are more regular than those in the Y_3TaO_7-type structure. In addition, the TaO_6 octahedra in the La_3NbO_7-type and Y_3TaO_7-type structure are tilted along the ⟨010⟩ and ⟨100⟩ direction, respectively. As described later, with increasing temperature, the Nd_3TaO_7 compound transforms from the Y_3TaO_7-type to La_3NbO_7-type structure at around RT.

Figure 3(a) shows the variation of lattice parameters $a/\sqrt{2}$ ($a \times \sqrt{2}$ for the defect-fluorite-type phase), b, and c of the RE_3TaO_7 series with the ionic radius of RE^{3+}. For convenience, the ionic radii for 8-coordinated RE^{3+} ions by Shannon [24] are adopted. With the RE^{3+} ionic radius, the lattice parameters tend to increase, and the differences among the $a/\sqrt{2}$, b, and c values become wide. For the Y_3TaO_7-type phases, the b values are almost equal to the c values between RE = Gd and Ho, and the b values become smaller than the c values between RE = Nd and Eu. The differences among $a/\sqrt{2}$, b, and c for the La_3NbO_7-type phases are more conspicuous than those for the Y_3TaO_7-type phases.

Figure 3(b) shows the variation of the averages of the RE(1)–O, RE(2)–O, and Ta–O interatomic distances for the weberite-type phases and the (RE, Ta)–O distances for the defect-

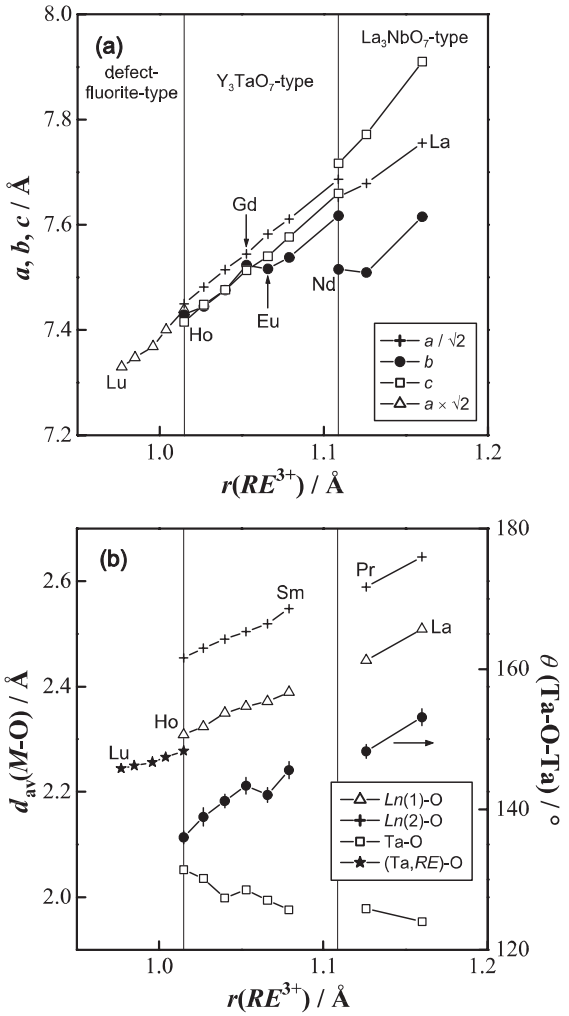

Figure 3. (a) Variation of lattice parameters $a/\sqrt{2}$ ($a \times \sqrt{2}$ for the defect-fluorite-type phase), b, and c for RE_3TaO_7 with ionic radius of 8-coordinated RE^{3+}. (b) Variation of the averages of the RE(1)–O, RE(2)–O, Ta–O interatomic distances for the weberite-type phases, and the (RE, Ta)–O distances for the defect-fluorite-type phase. Closed circles show the Ta–O(3)–Ta bond angles for the La_3NbO_7-type phase and the Ta–O(5)–Ta bond angles for the Y_3TaO_7-type phase.

fluorite-type phases. The RE(1)–O and RE(2)–O distances increase with increasing RE^{3+} ionic radius, while the Ta–O distances decrease. In addition to the interatomic distances, the Ta–O(3)–Ta bond angles for the La_3NbO_7-type phases and the Ta–O(5)–Ta bond angles for the Y_3TaO_7-type phases are also plotted as closed circles in figure 2(b). These angles correspond to the tilting angles of TaO_6 octahedra in the weberite-type compounds. Thus, the increase in the Ta–O–Ta angles with RE^{3+} ionic radius indicates that the tilt between the TaO_6 octahedra decreases in the weberite-type compounds containing larger RE^{3+} ions.

The Nd_3TaO_7 compound was reported to crystallize in the Y_3TaO_7-type structure with the space group $C222_1$ [5, 6]. Figure 1(d) shows the XRD profile of Nd_3TaO_7 at RT, indicating that the La_3NbO_7-type and Y_3TaO_7-type phases coexist at RT. The ratio of these two phases at RT was independent of the heating temperature (1673–1873 K) and cooling rate (quenching in air or gradual cooling in a furnace) for preparations. For these XRD measurements, we assumed that the Nd_3TaO_7 compounds showed the structural transition from the low symmetric Y_3TaO_7-type to the high symmetric La_3NbO_7-type phase with increasing temperature, and that both the La_3NbO_7-type and Y_3TaO_7-type phases were in metastable states at around RT.

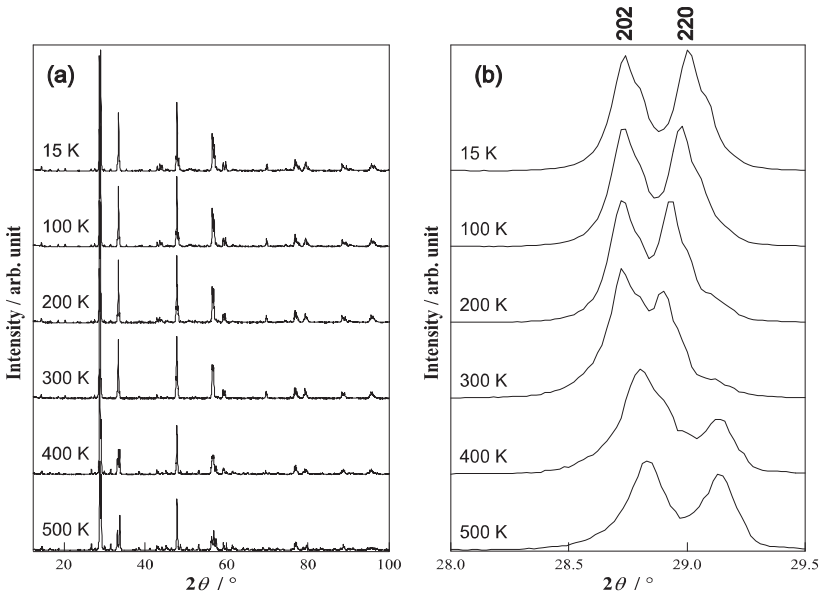

Figure 4. (a) XRD profiles of Nd_3TaO_7 at various temperatures. (b) The profiles in the range of $28° \leqslant 2\theta \leqslant 29.5°$.

In order to confirm this assumption, XRD measurements on Nd_3TaO_7 were performed on heating the sample from 15 to 500 K. The XRD profiles of Nd_3TaO_7 at 15, 100, 200, 300, 400, and 500 K are shown in figure 4(a). Figure 4(b) shows the profiles around the (220) and (202) reflections at the same temperature. The profiles above 440 K reveal that Nd_3TaO_7 transform to a single La_3NbO_7-type phase, while those below 170 K indicate that a single Y_3TaO_7-type phase appears. Table 3 lists the lattice and positional parameters at 100 and 500 K refined by the Rietveld method. With increasing temperature, the amount of the La_3NbO_7-type phase increase and the Y_3TaO_7-type phase disappears above 170 K. It can be concluded that this structural transition for Nd_3TaO_7 is a first order phase transition and that a superheating occurs over an exceedingly wide range of 270 K. In previous studies [5, 6], the Nd_3TaO_7 product was identified to have the Y_3TaO_7-type phase from only the Miller indices for the diffraction profiles. The space group $C222_1$ (Y_3TaO_7-type Nd_3TaO_7) is a subspace group of $Cmcm$ (La_3NbO_7-type Nd_3TaO_7) and the extinction rule of $C222_1$ is involved in that of $Cmcm$. As an example, the 201 reflection ($h0l$ with even h and odd l) is observed at $2\theta \sim 20.5°$ in the diffraction profiles for the Y_3TaO_7-type phase, while this reflection is not found in that for the La_3NbO_7-type phase (see figure 1). Thus, in the case that the diffraction profiles for the La_3NbO_7 and Y_3TaO_7-type phases overlap with each other, it becomes difficult to confirm the existence of the La_3NbO_7 phase by using only the Miller indices. Therefore, we suppose that the La_3NbO_7-type phase of Nd_3TaO_7 studied previously [5, 6] could have been overlooked (about 20% of the total Nd_3TaO_7).

To investigate the structural transition for other RE_3TaO_7 compounds, the XRD data of Pr_3TaO_7 (La_3NbO_7-type at RT), which was expected to transform to the Y_3TaO_7-type phase at low temperatures, were collected at 15 K, as shown in figure 5(b). The XRD data of Sm_3TaO_7 (Y_3TaO_7-type at RT), which was expected to transform to the La_3NbO_7-type phase at high temperatures, were also collected at RT and 500 K (see figure 5(d)). These profiles for Pr_3TaO_7 and Sm_3TaO_7 indicate that no evidence for any structural transition from Y_3TaO_7-type to La_3NbO_7-type phase was found in the measurable temperature region.

Table 3. Crystal structure data for Nd_3TaO_7. (Note: $R_{wp} = \left[\sum w(|F(o)|-|F(c)|)^2/\sum w|F(o)|^2\right]^{1/2}$ and $R_I = \sum |I_k(o) - I_k(c)|/\sum I_k(o)$.)

	Site	x	y	z	B (Å^2)
500 K Space group: $Cmcm$ $a = 10.9141(4)$ Å, $b = 7.5160(3)$ Å, $c = 7.6541(3)$ Å $R_I = 2.80\%$, $R_{wp} = 13.40\%$					
Nd(1)	4a	0	0	0	0.71(4)
Nd(2)	8g	0.2291(1)	0.2936(2)	1/4	0.71
Ta	4b	0	1/2	0	0.20(5)
O(1)	4c	0	0.434(3)	1/4	0.7(2)
O(2)	16h	0.1229(9)	0.316(2)	−0.033(1)	0.7
O(3)	8g	0.136(1)	0.024(2)	1/4	0.7
100 K Space group: $C222_1$ $a = 10.8411(4)$ Å, $b = 7.5997(3)$ Å, $c = 7.6954(3)$ Å $R_I = 4.51\%$, $R_{wp} = 13.08\%$					
Nd(1)	4b	0	0.5004(2)	1/4	0.97(5)
Nd(2)	8c	0.2326(2)	0.2339(2)	0	0.97
Ta	4b	0	0	1/4	0.40(6)
O(1)	8c	0.140(1)	0.184(1)	0.272(1)	0.7(1)
O(2)	8c	0.139(1)	0.812(1)	0.281(1)	0.7
O(3)	4a	0.120(1)	1/2	0	0.7
O(4)	4a	0.136(1)	1/2	1/2	0.7
O(5)	4a	0.037(1)	0	0	0.7

3.2. Paramagnetic behaviour

For the RE_3TaO_7 compounds, the magnetic behaviour originates from only the magnetic RE ions. Magnetic susceptibility measurements for RE_3TaO_7 except for RE = Nd, Tb, Dy, and Ho (Y_3TaO_7-type phase) show paramagnetic behaviour down to 1.8 K. The Sm_3TaO_7 and Eu_3TaO_7 compounds show the well-known van Vleck paramagnetism caused by the behaviour of Sm^{3+} and Eu^{3+} ions [25].

The temperature dependences of the reciprocal magnetic susceptibilities (χ^{-1}) of Gd_3TaO_7 and Yb_3TaO_7 are shown in figure 6. For both Gd_3TaO_7 and Yb_3TaO_7, no evidence of any magnetic transition has been recognized down to 1.8 K. The reciprocal susceptibilities of Yb_3TaO_7 exhibit Curie–Weiss behaviour between 200 and 300 K, but deviate from the Curie–Weiss law below 200 K, while those of Gd_3TaO_7 obey the Curie–Weiss law above 5 K. The Gd^{3+} ion has the $^8S_{7/2}$ ground state without orbital momentum, so the crystal electric field (CEF) does not affect the susceptibility of the Gd^{3+} ions. On the other hand, the $^2F_{7/2}$ ground state of the Yb^{3+} ion should be split into three levels, Γ_6 doublet ($m \sim 1.33\ \mu_B$; $\mu_{eff} \sim 2.02\ \mu_B$), Γ_7 doublet ($m \sim 1.71\ \mu_B$; $\mu_{eff} \sim 2.46\ \mu_B$), and Γ_8 quartet ($1.7\ \mu_B \leqslant m \leqslant 2.1\ \mu_B$; $2.5\ \mu_B \leqslant \mu_{eff} \leqslant 2.9\ \mu_B$), in the cubic T_d symmetry for the ideal fluorite-type structure. The effective magnetic moments (μ_{eff}) per Yb^{3+} ion and the Weiss constant (θ) were obtained to be 3.49(1) μ_B and −2.79(2) K, respectively, from the Curie–Weiss fitting to the χ^{-1}–T curve in the temperature range between 5 and 10 K. This moment is considerably higher than the expected effective moments of every state (Γ_6, Γ_7, Γ_8), and we could not simply determine the lowest level. In the defect-fluorite-type Yb_3TaO_7, the Yb-site symmetry is suggested to become

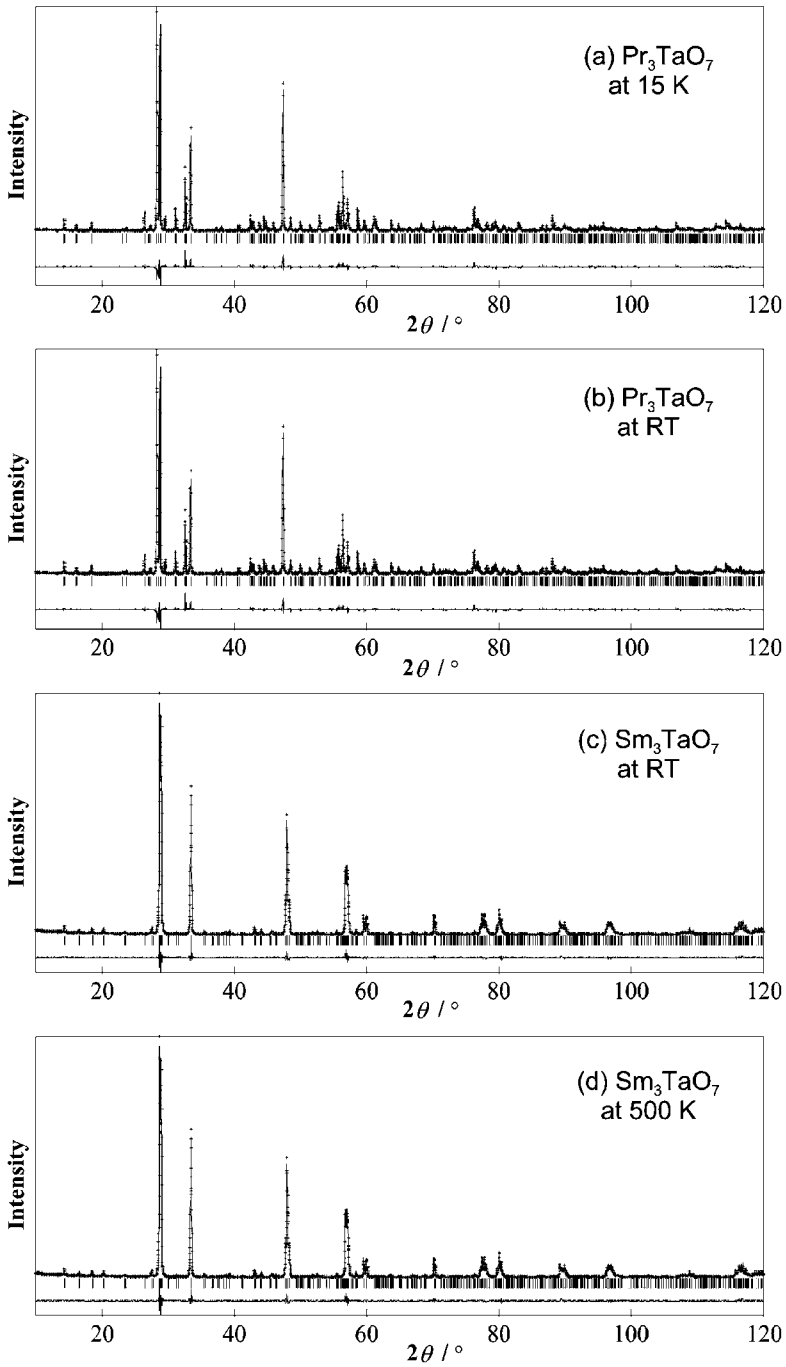

Figure 5. XRD profiles of Pr_3TaO_7 at 15 K (a), RT (b) and Sm_3TaO_7 at RT (c), 500 K (d).

lower than the T_d symmetry by local distortions which are attributable to disordering of cations and defects of anions. Such a CEF effect on Yb^{3+} causes the large deviation from the Curie–Weiss law below 200 K. From the Curie–Weiss law fitting to the χ^{-1}–T curves, μ_{eff} per RE ion

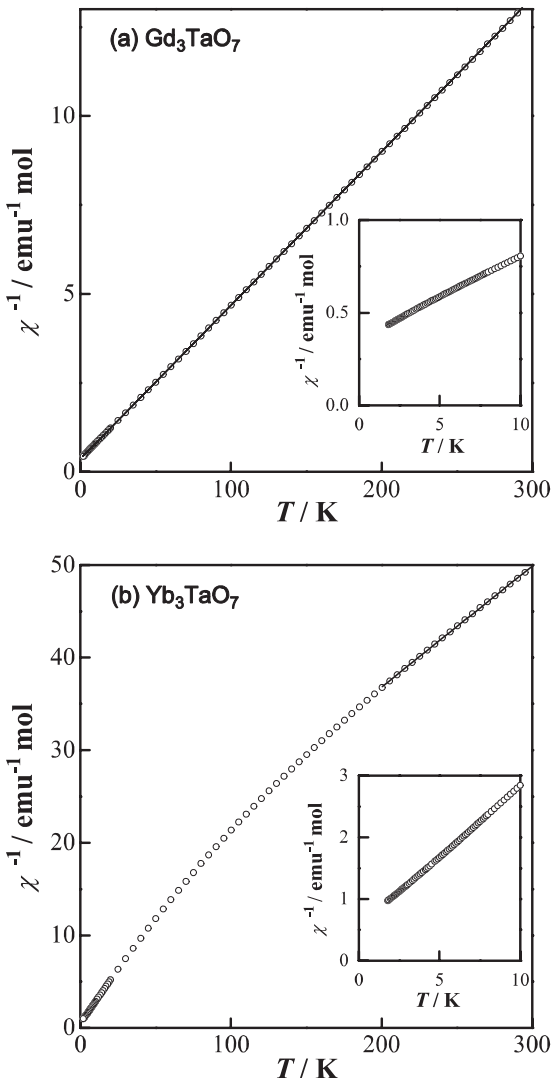

Figure 6. Temperature dependence of the reciprocal magnetic susceptibility χ^{-1} of (a) Gd_3TaO_7 and (b) Yb_3TaO_7.

was estimated to be 7.87(1) μ_B for Gd_3TaO_7 (5 K $\leqslant T \leqslant$ 300 K) and 4.52(1) μ_B for Yb_3TaO_7 (200 K $\leqslant T \leqslant$ 300 K). These effective magnetic moments agree well with the theoretical moments for a free Gd^{3+} ($\mu_{eff} = 7.94\ \mu_B$ for $g = 2$ and $S = 7/2$) and Yb^{3+} ($\mu_{eff} = 4.54\ \mu_B$ for $g_J = 8/7$ and $J = 7/2$) ions. The negative Weiss constants (−8.60 K for Gd_3TaO_7 and −2.79 K for Yb_3TaO_7) are presumably due to antiferromagnetic exchange coupling among Gd^{3+} (Yb^{3+}) moments. If the magnetic susceptibility measurements were carried out further below 1.8 K, both Gd_3TaO_7 and Yb_3TaO_7 should show an antiferromagnetic transition or a Schottky-like anomaly due to the $^8S_{7/2}$ ground state of Gd^{3+} and a low-lying Kramers doublet of Yb^{3+}, respectively.

For all the RE_3TaO_7 (except for RE = Sm and Eu) compounds, the temperature dependence of the magnetic susceptibilities obeys the Curie–Weiss law in the high temperature

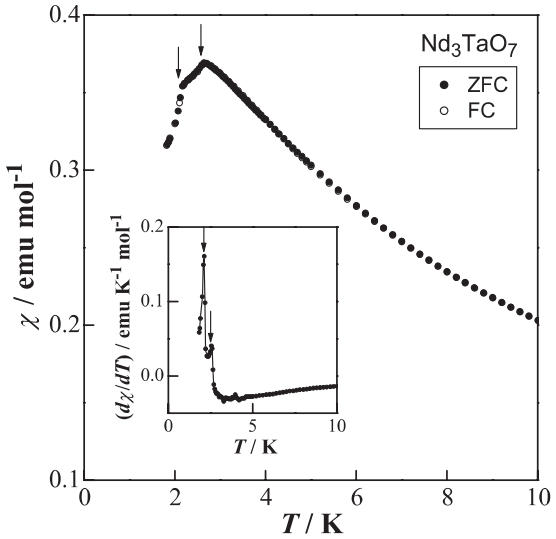

Figure 7. Temperature dependence of the magnetic susceptibility χ for Nd_3TaO_7. The inset shows the first derivatives of χ.

Table 4. Magnetic properties of RE_3TaO_7.

RE	Magnetic properties	T_N	μ_{eff} (obs.) (μ_B)		μ_{eff} (calc.) (μ_B)
Pr	Curie–Weiss	—	3.08(1)	(200–300 K)	3.58
Nd	Antiferro	2.1, 2.6	3.39(2)	(200–300 K)	3.62
Sm	van Vleck	—		—	—
Eu	van Vleck	—		—	—
Gd	Curie–Weiss	—	7.87(1)	(5–300 K)	7.94
Tb	Antiferro	2.9, 3.6	9.54(1)	(100–300 K)	9.72
Dy	Antiferro	2.3	10.37(1)	(100–300 K)	10.65
Ho	Weak ferro	2.6	10.44(2)	(100–300 K)	10.62
Ho	Curie–Weiss	—	10.29(1)	(100–300 K)	10.62
Er	Curie–Weiss	—	9.44(1)	(100–300 K)	9.58
Tm	Curie–Weiss	—	7.38(2)	(100–300 K)	7.56
Yb	Curie–Weiss	—	4.52(1)	(200–300 K)	4.54

region. The effective magnetic moments per RE ion calculated from the Curie–Weiss fitting agree well with the theoretical moments for a free trivalent RE ion. Table 4 summarizes the results of the magnetic susceptibility measurements.

3.3. Magnetic ordering

3.3.1. Nd_3TaO_7. Figure 7 shows the temperature dependence of the magnetic susceptibilities (χ) of Nd_3TaO_7 below 10 K. An antiferromagnetic transition is observed at 2.6 K and the absence of divergence between the ZFC and FC magnetic susceptibilities indicates that the Nd^{3+} ions are in an antiferromagnetic state without any weak ferromagnetic properties below 2.6 K. However, below the Néel temperature, the fall of the χ values with decreasing temperature seems to be constituted of two-step abrupt drops, as shown in figure 7. To clarify this anomaly, the first derivative of the magnetic susceptibility ($d\chi/dT$) was calculated and it is shown in the inset of figure 7. Two peaks are observed at 2.1 and 2.6 K. This result suggests that the

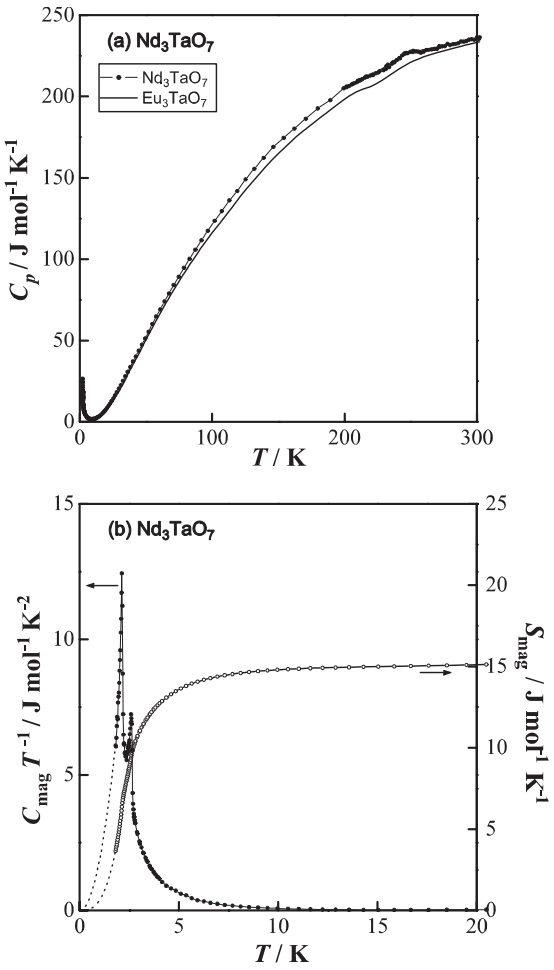

Figure 8. (a) Temperature dependence of the specific heat C_p for Nd_3TaO_7 and Eu_3TaO_7 below 300 K. (b) Temperature dependence of C_{mag}/T and S_{mag} for Nd_3TaO_7.

Nd^{3+} ions occupying the nonequivalent 4b and 8c sites (RE(1) and RE(2) sites in figure 2(d)) individually transform to the antiferromagnetic states in the Nd_3TaO_7 compound.

Figure 8(a) shows the temperature dependence of the specific heat (C_p) of Nd_3TaO_7 below 300 K. In order to estimate the magnetic contribution (C_{mag}) to C_p, we need to subtract the lattice contribution (C_{lat}) and the electronic contribution ($C_e \sim 0$ J mol^{-1} K^{-1} for insulators) from the total C_p. The C_p data for insulating Eu_3TaO_7, which is isostructural with the low-temperature Nd_3TaO_7 phase (Y_3TaO_7-type), are also plotted in the same figure (figure 8(a)). For the Eu^{3+} ions, the energy difference between the ground state ($^7F_0$) and the first excited state ($^7F_1$) is roughly 500 K [25]. Therefore, we can assume that the population of the 'nonmagnetic' $^7F_0$ state is predominant at low temperatures below 20 K and that the Schottky-type specific heat contributions, which are attributable to the excited states ^7F_J ($J = 1, 2, \ldots, 6$), to the total C_p of Eu_3TaO_7 are negligible below 20 K. Thus, because the C_{lat} contributions to the total C_p of Eu_3TaO_7 are almost the same as that of Nd_3TaO_7 below 20 K, the C_{mag} for Nd_3TaO_7 is obtained by subtracting the total C_p ($\sim C_{lat}$) of Eu_3TaO_7 from the ($\sim C_{mag} + C_{lat}$) of Nd_3TaO_7. The temperature dependences of C_{mag}/T and the magnetic entropy ($S_{mag} = \int_0^T (C_{mag}/T')\,dT'$) below 20 K are shown in figure 8(b). According to the antiferromagnetic spin-wave model, C_{mag} is expected to be proportional to T^3 at $T < T_N$ [26]. The calculated values of C_{mag}/T

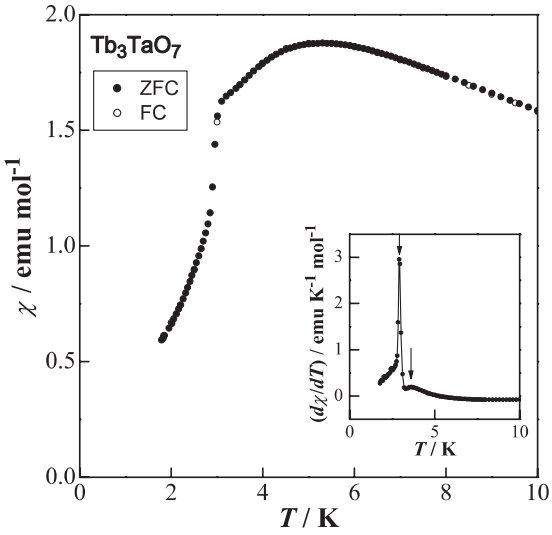

Figure 9. Temperature dependence of the magnetic susceptibility χ for Tb_3TaO_7. The inset shows the first derivatives of χ.

and S_{mag} below 1.8 K are also plotted as a broken line in figure 8(b). In the C_{mag}/T versus T curve, the C_{mag}/T increases gradually with decreasing temperature below 10 K and two λ-type anomalies appear at 2.1 and 2.6 K. These peak temperatures agree with the peak temperatures in the $d\chi/dT$–T curve of figure 7. From the S_{mag}–T curve, the magnetic entropy change at 10 K is estimated to be 14.8 J mol^{-1} K^{-1}. Per Nd_3TaO_7 chemical formula, one Nd^{3+} ion occupies the RE(1) (4b) site and two Nd^{3+} ions the RE(2) (8c) site in figure 2(d). The $^4I_{9/2}$ ground state of the Nd^{3+} ion occupying these sites should split into five Kramers doublets by the CEF in the orthorhombic symmetry. In the antiferromagnetic state, only the lowest doublets of the Nd^{3+} ions need to be considered, because S_{mag} approaches $3R\ln 2 \sim 17.3$ J mol^{-1} K^{-1} ($R\ln 2$ per mole of Nd^{3+} ion), where R is the gas constant. Owing to the difficulty in separating two λ-type peaks of C_{mag}/T, we hardly estimate the individual C_{mag} contributions originated from the Nd^{3+} ions at the RE(1) and RE(2) sites. However, considering the result that the peak value of C_{mag}/T at 2.1 K is about twice as large as that at 2.6 K, we believe that the antiferromagnetic transitions at 2.6 and 2.1 K are due to the magnetic interactions between Nd^{3+} ions occupying the RE(1) and RE(2) sites, respectively, because one-third of the Nd^{3+} ions are situated at the RE(1) sites and two-thirds of the Nd^{3+} ions are situated at the RE(2) sites.

3.3.2. Tb_3TaO_7. Figure 9 shows the temperature dependence of the magnetic susceptibilities of Tb_3TaO_7 below 10 K. The χ of Tb_3TaO_7 shows a broad maximum at around 5 K and drops abruptly below 3.0 K. The magnetic behaviour of this compound shows no divergence between the ZFC and FC magnetic susceptibilities. Thus, all the Tb^{3+} ions are found to be in an antiferromagnetic state without any weak ferromagnetic component below 3.0 K. The inset of figure 9 shows $d\chi/dT$ for Tb_3TaO_7. The feature of this $(d\chi/dT)$–T curve for Tb_3TaO_7 is similar to that for Nd_3TaO_7. With decreasing temperature, $d\chi/dT$ increases gradually below 6 K, and a sharp peak and a broad small peak are observed at 2.9 and 3.6 K, respectively.

The temperature dependences of C_{mag}/T and S_{mag} of Tb_3TaO_7 were derived in a manner identical with those of Nd_3TaO_7, and they are shown in figures 10(a) and (b). C_{mag}/T increases gradually with decreasing temperature below 15 K, and a sharp λ-type anomaly and a small peak are observed at 2.9 and 3.6 K, respectively. For the Tb_3TaO_7 compound, it is suggested that a long-range antiferromagnetic ordering of the Tb^{3+} ions occupying each site (RE(1) and

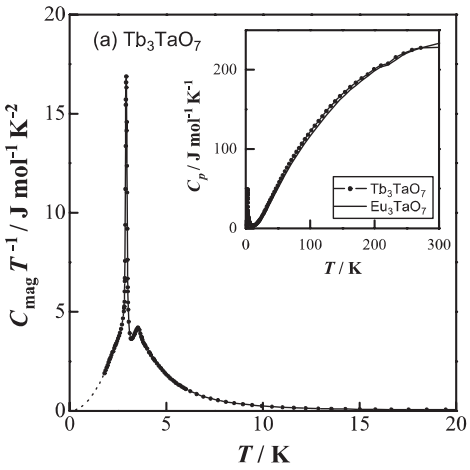

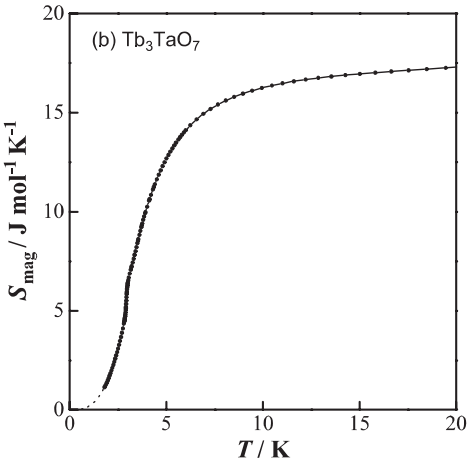

Figure 10. (a) Temperature dependence of C_{mag}/T for Tb_3TaO_7. The inset shows the temperature dependence of C_p of Tb_3TaO_7 below 300 K. (b) Temperature dependence of S_{mag} of Tb_3TaO_7.

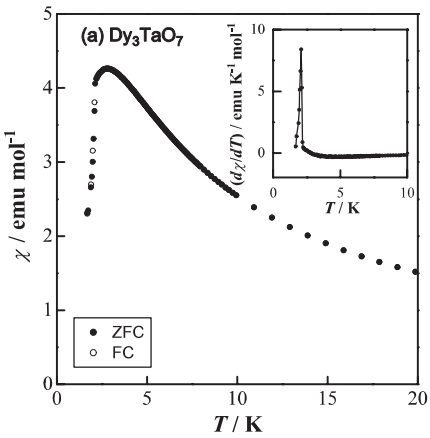

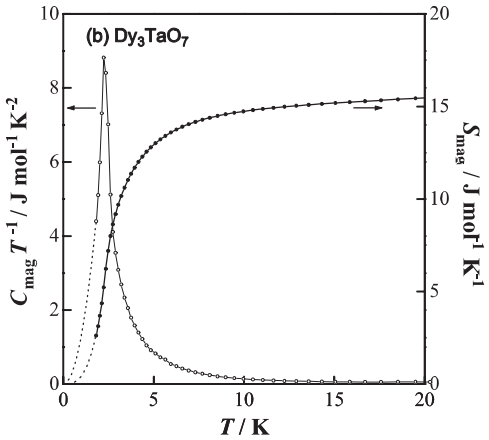

Figure 11. (a) Temperature dependence of the susceptibility χ for Dy_3TaO_7. The inset shows the first derivatives of χ. (b) Temperature dependence of C_{mag}/T and S_{mag} for Dy_3TaO_7.

RE(2)) individually occurs at 2.9 and 3.6 K and a short range magnetic ordering begins below about 15 K. S_{mag} converges to $3R\ln 2$ (see figure 10(b)), which indicates that the ground $^7F_6$ state of the Tb^{3+} ion is split by the CEF and that the antiferromagnetic ordering of the Tb^{3+} ions is caused by only the non-Kramers ground doublet.

3.3.3. Dy_3TaO_7. Figure 11(a) shows the temperature dependence of the magnetic susceptibilities for Dy_3TaO_7 below 20 K. A broad peak and an abrupt drop are observed at around 2.8 K and below 2.1 K, respectively. No ferromagnetic behaviour is found below the Néel temperature. The calculated $d\chi/dT$ curve for Dy_3TaO_7 shows a simple antiferromagnetic transition. The temperature dependences of C_{mag}/T and S_{mag} of Dy_3TaO_7 are plotted in figure 11(b). C_{mag} for Dy_3TaO_7 is obtained by subtracting the total C_p of Eu_3TaO_7 from that of Dy_3TaO_7. A λ-type anomaly is observed at 2.3 K and S_{mag} converges to $3R\ln 2$. The antiferromagnetic ordering of the Dy^{3+} ions is suggested to be attributable to only the Kramers

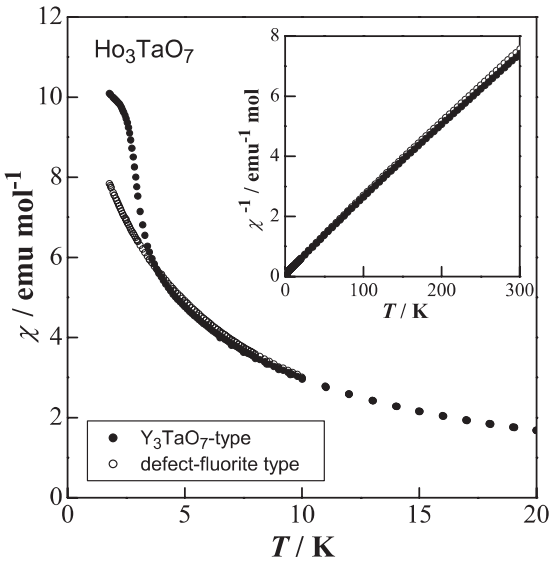

Figure 12. Temperature dependence of the susceptibility χ of Ho_3TaO_7 with the Y_3TaO_7-type and defect-fluorite-type structures below 20 K. The inset shows the temperature dependence of χ^{-1}.

ground doublet, which is derived from the ground $^6G_{15/2}$ state of Dy^{3+} by the CEF splitting. These χ–T and C_{mag}/T–T curves reveal that the antiferromagnetic ordering of the Dy^{3+} ions occupying the RE(1) and RE(2) sites occurs at the same temperature.

3.3.4. Ho_3TaO_7. In the case of the Ho compound, the magnetic susceptibility and specific heat measurements were carried out for two different phases (Y_3TaO_7-type and defect-fluorite-type). Figure 12 shows the χ–T curves of the Y_3TaO_7-type and defect-fluorite-type Ho_3TaO_7 below 20 K. The χ^{-1}–T curves are also depicted in the inset of figure 12. A notable discrepancy in the susceptibilities between the Y_3TaO_7-type and defect-fluorite-type Ho_3TaO_7 is not found above 10 K. However, the Y_3TaO_7-type Ho_3TaO_7 shows a rise of χ below 3 K with decreasing temperature, while the χ of the defect-fluorite-type Ho_3TaO_7 demonstrates Curie–Weiss behaviour down to 1.8 K. This magnetic anomaly for the Y_3TaO_7-type Ho_3TaO_7 may be ferrimagnetic or weak ferromagnetic.

Figures 13(a)–(c) show the temperature dependences of C_p and C_{mag}/T for the Y_3TaO_7-type and defect-fluorite-type Ho_3TaO_7. In a similar manner as the case of Nd_3TaO_7, the C_{mag} values for Y_3TaO_7-type and defect-fluorite-type Ho_3TaO_7 are obtained by subtracting the total C_p of Eu_3TaO_7 and Lu_3TaO_7 from those of Ho_3TaO_7, respectively. A λ-type anomaly is observed at 2.6 K in the C_{mag}/T–T curve of the Y_3TaO_7-type Ho_3TaO_7 (figure 13(a)), and this temperature corresponds to the temperature of the anomaly in the χ–T curve. C_{mag}/T–T of the defect-fluorite-type Ho_3TaO_7 increases with decreasing temperature below 20 K (figure 13(b)). This behaviour is due to the magnetic ordering of Ho^{3+} which will occur below 1.8 K.

In order to elucidate the magnetic anomaly of the Y_3TaO_7-type Ho_3TaO_7, the magnetization was measured under magnetic fields from 0 to 9 T at both 1.8 and 5 K, and the results are shown in figure 14. No remanent magnetization is observed in the M–H curve at 1.8 K. The M–H curves at 1.8 and 5 K could not be described by the Brillouin function for a free Ho^{3+} ($^5I_8$) ion with $g_J = 5/4$ and $J = 8$. The magnetization, ∼16 μ_B, at 9 T is roughly half the theoretical magnetization (=30 μ_B). Similar behaviour has been observed in the Ho^{3+} compounds and it is thought to be due to a single ion anisotropy of Ho^{3+} [27–30]. On the assumption that the ground state is an effective spin one-half doublet ($S = 1/2$) with effective

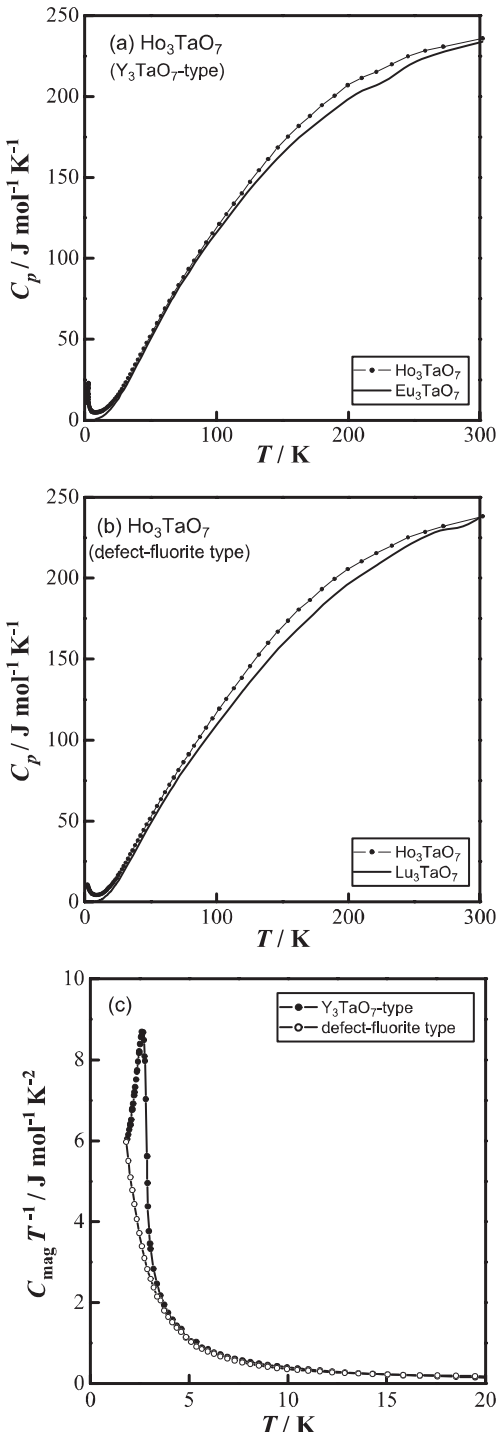

Figure 13. (a) Temperature dependence of C_p of Y_3TaO_7-type Ho_3TaO_7 and Eu_3TaO_7 below 300 K. (b) Temperature dependence of C_p of defect-fluorite-type Ho_3TaO_7 and Lu_3TaO_7 below 300 K. (c) Temperature dependence of C_{mag}/T of the Y_3TaO_7-type and defect-fluorite-type Ho_3TaO_7 below 20 K.

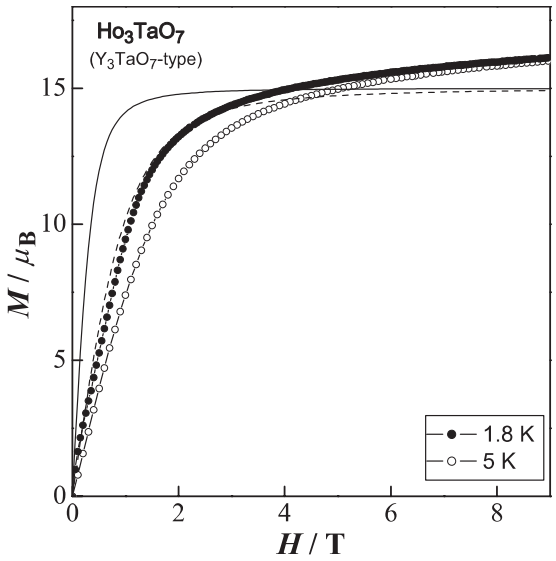

Figure 14. Magnetization as a function of the magnetic field at 1.8 and 5 K for Ho_3TaO_7 with the Y_3TaO_7-type structure. The solid curve is the theoretical magnetization curve at 1.8 K and the broken line is that at 5 K (see text).

g_{eff} value, the temperature and field dependences of the powder-averaged magnetization $\langle\mu\rangle$ is expressed by the following equation [27]:

$$\langle\mu\rangle/\mu_{\mathrm{B}} = \frac{(kT)^2}{g_{\mathrm{eff}} S(\mu_{\mathrm{B}} H)^2} \int_0^{g_{\mathrm{eff}} S\mu_{\mathrm{B}} H/kT} x \tanh x \, \mathrm{d}x,$$

where $g_{\parallel} = g_{\mathrm{eff}}$, $g_{\perp} = 0$ with $\parallel$ and $\perp$ denoting parallel and perpendicular to the applied field, respectively. In figure 14, the solid and broken lines represent the theoretical magnetization for a ground doublet ($S = 1/2$, $g_{\mathrm{eff}} = 20$) with an easy-axis anisotropy at 1.8 and 5 K, respectively. This effective g value ($g_{\mathrm{eff}} = 20$) is the corresponding maximum value with a well isolated non-Kramers $J_z = \pm 8$ doublet. We have ignored the exchange coupling among the Ho^{3+} moments in the above equation. The gentle slope at low magnetic fields in the observed M–H curve compared with that for the theoretical M–H curve is indicative of the antiferromagnetic exchange coupling among the Ho^{3+} moments. Thus, it is suggested that the magnetic anomaly observed at 2.6 K for the Y_3TaO_7-type Ho_3TaO_7 is an antiferromagnetic ordering of Ho^{3+} with very weak ferromagnetic components.

4. Conclusion

Crystal structures and magnetic properties of rare earth tantalates RE_3TaO_7 (RE = rare earths) have been studied. The x-ray diffraction measurements indicate that Nd_3TaO_7 transforms from Y_3TaO_7-type to La_3NbO_7-type with temperature at around RT. For the Nd and Tb compounds, their magnetic susceptibility measurements show that the magnetic moments of the RE(1) and RE(2) sites become antiferromagnetic state individually. The Dy^{3+} ion is found to be in a simple antiferromagnetic state below 2.3 K. The Ho_3TaO_7 with the Y_3TaO_7-type structure shows a weak ferromagnetic transition, while no magnetic ordering is observed down to 1.8 K for the defect-fluorite-type Ho_3TaO_7. It is suggested that the magnetic ordering of Nd^{3+}, Tb^{3+}, Dy^{3+} and Ho^{3+} is ascribed to the low-lying doublets.

References

[1] Rooksby H P and White E A D 1964 *J. Am. Ceram. Soc.* **47** 94
[2] Bondar N A, Kalinin A I and Koroleva L L 1972 *Inorg. Mater.* **8** 1649
[3] Isupova E N, Savchenko E P and Keler E K 1975 *Inorg. Mater.* **11** 1201
[4] Wirkus C D, Schidecker R W and Wilder D R 1977 *Mater. Res. Bull.* **12** 367
[5] Yokogawa Y and Yoshimura M 1997 *J. Am. Ceram. Soc.* **80** 1965
[6] Allpress J G and Rossell H J 1979 *J. Solid State Chem.* **27** 105
[7] Yoshimura M, Yokogawa Y and Somiya S 1983 *Yogyo Kyokaishi* **93** 593
[8] Yoshimura M, Yokogawa Y and Somiya S 1989 *Solid State Ion.* **28–30** 1250
[9] van Berkel F P F and IJdo D J W 1986 *Mater. Res. Bull.* **21** 1103
[10] Vente J F and IJdo D J W 1991 *Mater. Res. Bull.* **26** 1255
[11] Vente J F, Helmholdt R B and IJdo D J W 1994 *J. Solid State Chem.* **108** 18
[12] Greedan J E, Raju N P, Wegner A, Gougeon P and Padiou J 1997 *J. Solid State Chem.* **129** 320
[13] Khalifah P, Erwin R W, Lynn J W, Huang Q, Batlogg B and Cava R J 1999 *Phys. Rev.* B **60** 9573
[14] Wiss F, Raju N P, Wills A S and Greedan J E 2000 *Int. J. Inorg. Mater.* **2** 53
[15] Bontchev R P, Jacobson A J, Gospodinov M M, Skumryev V, Popov V N, Lorenz B, Meng R L, Litvinchuk A P and Iliev M N 2000 *Phys. Rev.* B **62** 12235
[16] Harada D and Hinatsu Y 2001 *J. Solid State Chem.* **158** 245
[17] Harada D, Hinatsu Y and Ishii Y 2001 *J. Phys.: Condens. Matter* **13** 10825
[18] Harada D and Hinatsu Y 2002 *J. Solid State Chem.* **164** 163
[19] Zhou Z X, Cao G, McCall S, Crow J E, Guertin R P, Mielke C H and Rickel D G 2002 *Phil. Mag.* B **82** 1401
[20] Plaisier J R, Drost R J and IJdo D J W 2002 *J. Solid State Chem.* **169** 189
[21] Lam R, Langet T and Greedan J E 2003 *J. Solid State Chem.* **171** 317
[22] Nishimine H, Wakeshima M and Hinatsu Y 2004 *J. Solid State Chem.* **177** 739
[23] Izumi F and Ikeda T 2000 *Mater. Sci. Forum* **321–324** 198–203
[24] Shannon R D 1976 *Acta Crystallogr.* A **32** 751
[25] van Vleck J H 1932 *Theory of Electric and Magnetic Susceptibilities* (Oxford: Clarendon)
[26] Joshua S J and Cracknell A P 1969 *Phys. Lett.* A **28** 562
[27] Flood D J 1974 *J. Appl. Phys.* **45** 4041
[28] Bramwell S T, Field M N, Harris M J and Parkin I P 2000 *J. Phys.: Condens. Matter* **12** 483
[29] Jana Y M and Ghosh D 2000 *Phys. Rev.* B **61** 9657
[30] Cornelius A L and Gardner J S 2001 *Phys. Rev.* B **64** 60406